Quasi-10-day wave activity in the southern high-latitude MLT region and its relation to the large-scale instability and gravity wave drag

Wonseok Lee[1], In-Sun Song[1], Byeong-Gwon Song[1], Yong Ha Kim[2]

[1]Department of Atmospheric Sciences, Yonsei University, Seoul 03722, South Korea

[2]Department of Astronomy and Space Science, Chungnam National University, Daejeon 34134, South Korea

Correspondence to: In-Sun Song (songi@yonsei.ac.kr)

Abstract. Seasonal variation of westward-propagating quasi-10-day wave (Q10DW) in the mesosphere and lower thermosphere of the Southern Hemisphere (SH) high-latitude regions is investigated using meteor radar (MR) observations for the period of 2012–2016 and Specified Dynamics (SD) version of the Whole Atmosphere Community Climate Model (WACCM). The phase difference of meridional winds measured by two MRs located in Antarctica gives observational estimates of the amplitude and phase of Q10DW with zonal wavenumber 1 (W1). The amplitude of the observed Q10DW-W1 is large around equinoxes. In order to elucidate the variations of the observed Q10DW-W1 and its possible amplification mechanism, we carry out two SD-WACCM experiments nudged towards the MERRA-2 reanalysis from the surface up to ~60 km (EXP60) and ~75 km (EXP75). Results of the EXP75 indicate that the observed Q10DW-W1 can be amplified around the barotropic/baroclinic instability regions in the middle mesosphere around 60°S–70°S. In the EXP60, it is also found that Q10DW-W1 is amplified around the instability regions, but the amplitude is too large compared with MR observations. The large-scale instability in the EXP60 in the SH summer mesosphere is stronger than that in the EXP75 and Microwave Limb Sounder observation. The larger instability in the EXP60 is related to the large meridional and vertical variations of polar mesospheric zonal winds in association with gravity wave parameterization (GWP). Given uncertainties inherent in GWP, these results can suggest that it is possible for models to spuriously generate traveling planetary waves such as Q10DW, especially in summer, due to the excessively strong large-scale instability in the SH high-latitude mesosphere.

2

1 Introduction

A series of Rossby normal modes (free oscillations) is the homogeneous solution of the governing equations on a sphere linearized with respect to the isothermal and quiescent reference atmosphere (e.g., Andrews et al., 1987; Forbes et al., 1995; Salby, 1984). Traveling normal modes exhibit clear planetary-scale spatiotemporal oscillations throughout the whole atmosphere, and for sufficiently large amplitudes, these traveling planetary waves (PWs) can play an important role in the momentum and energy transfer to the mean flow (Salby, 1984). Three gravest traveling normal modes have been observed: Westward-propagating zonal-wavenumber-1 PWs with periods of approximately 5, 10, and 16 days. The classical wave theory based on the isothermal and quiescent atmosphere gives the theoretical periods of 5, 8.3, and 12.5 day, but the periods in the real atmosphere can be shifted to values close to 5, 10, and 16 days, respectively (Salby, 1981a, b), due to influences of the vertical and meridional variation of the mean horizontal winds and temperature.

Among the gravest modes, the quasi-5-day wave (Q5DW) and quasi-16-day wave (Q16DW) have extensively been studied through observations, modeling, and assimilation products: Ground-based observations (e.g., Day and Mitchell, 2010; He et al., 2020b; Mitra et al., 2022), satellite observations (e.g., Forbes and Zhang, 2017; Huang et al., 2022), reanalysis data (e.g., Huang et al., 2017), and simulations (e.g., Qin et al., 2021). Using meteor radars (MRs) located in the northern and southern polar regions, Day and Mitchell (2010) showed that PW activity is strong during winter and the seasonal variation of PW is similar in both polar regions. According to Qin et al. (2021) and Mitra et al. (2022), the barotropic and baroclinic instabilities are the possible

3

57   sources of Q5DW and Q16DW in that the waves can draw energy from the mean flow

58   in the instability region. The disturbance of zonal-mean flow frequently occurs during

59   the large-scale meteorological events such as sudden stratospheric warming (SSW). It

60   has been reported that the amplitude of Q5DW or Q16DW increases during SSW events

61   (Eswaraiah et al., 2016; Lee et al., 2021; Li et al., 2021; Ma et al., 2022). In addition,

62   the amplified PWs can interact with tidal waves through the in-situ nonlinear

63   interaction, resulting ionospheric disturbances during SSW (e.g., Goncharenko et al.,

64   2020; Forbes et al., 2021; Liu et al., 2021; Qin et al., 2019).

65   In contrast, the westward propagating quasi-10-day wave (Q10DW) with zonal

66   wavenumber 1 (W1) has received little attention compared to the other gravest normal

67   modes. Forbes and Zhang (2015) showed that Q10DW-W1 has a mean period of $9.8 \pm$

68   0.4 days using the temperature measurements from the Sounding of the Atmosphere

69   using Broadband Emission Radiometry (SABER) instrument mounted on NASA's

70   TIMED (Thermosphere Ionosphere Mesosphere Energetics Dynamics) satellite in

71   2002–2013. They presented that the large amplitude of Q10DW-W1 is found in the

72   mid-latitude (40–50° latitude) mesosphere and lower thermosphere (MLT) region of

73   both hemispheres in equinoxes, although their results are limited to the latitude of 50°

74   because of the yaw cycle of the satellite. Hirooka (2000) reported that the global

75   structure of Q10DW-W1 using the Improved Stratosphere and Mesospheric Souder

76   (ISAMS) instrument aboard Upper Atmosphere Research Satellite (UARS) from

77   November 1991 to May 1992. The results also showed that the Q10DW-W1 is active

78   during equinoxes and winter at 0.1 hPa (~65 km). In addition, it is found that

79   nonuniform and background zonal wind field can influence the structure of the wave in

80   the mesosphere. The amplitude of the Q10DW-W1 is uniform or decays in the vertical

81 near the mesopause, and it does not increase above the mesosphere, even though the

82 critical layer is absent. Using the airglow intensities simulated by the global circulation

83 model assimilated by the reanalysis data from ground to 30 km, Egito et al. (2017) also

84 found that the 10-day oscillation is dominant from autumn to spring in the mid-latitude

85 MLT region. More recently, Huang et al. (2021) investigated the Q10DW activity based

86 on the Modern-Era Retrospective analysis for Research and Applications version 2

87 (MERRA-2) reanalysis data. They showed that the dominant components of Q10DW

88 are westward-propagating waves with zonal wavenumber 1 during winter and spring in

89 the stratosphere and mesosphere and eastward-propagating waves with zonal

90 wavenumber 1 and 2, which are excited in the mesospheric instability region. Although

91 both westward and eastward Q10DW modes are found, they mainly focus on the

92 eastward propagating Q10DW.

93   Several studies have investigated the response of Q10DW-W1 to SSWs.

94 Matthias et al. (2012) conducted a composite analysis of wave activities during major

95 Northern Hemisphere (NH) SSWs from 1989 to 1998, revealing an amplification of

96 Q10DW-W1 in the NH high-latitude MLT region following major SSW events. He et

97 al. (2022a, 2022b) utilized NH MRs to observe the occurrence of Q10DW-W1 and

98 Q16DW-W1 during four winter major SSWs. They found that these waves persisted for

99 approximately three to five whole cycles during the events. Chandran et al. (2013)

100 examined the forcing of secondary PWs-W1 driven by stratospheric instability on zonal

101 winds as a response to 2012 NH minor SSW. Sassi and Liu (2014) conducted numerical

102 simulations during minor and major NH SSWs and solar minimum condition. They

103 found that PWs-W1 with periods between 2 and 10 days originating in the high-latitude

104 NH could propagate equatorward and influence equatorially trapped tides. This

105 equatorward propagation of secondary PWs was also reported by Qin et al. (2022).

106 They suggested that secondary PWs-W1 with periods of 10 to 16 days generated in the

107 high-latitude NH during sudden stratospheric final warming could impact the Southern

108 Hemisphere (SH) stratosphere, depending on the phase of Quasi-Biennial Oscillation

109 (QBO). In the SH, studies by Lee et al. (2021) and Wang et al. (2021) using SH MRs

110 reported that Q10DW was amplified prior to 2019 SH SSW. Yamazaki and Matthias

111 (2019) reported that the Q10DW-W1 is not only intensified during SSWs but also

112 affected by seasonal timing of SSWs (i.e., final stratospheric warming) in stratospheric

113 instability regions.

114　　　　While the amplification mechanism of Q10DW-W1 generated following SSWs

115 has been addressed in previous studies (e.g., Qin et al., 2022, Yin et al., 2023), the

116 specific mechanisms driving their seasonal amplification during equinoxes remain less

117 explored. In the present study, we focus on the seasonal variation of Q10DW-W1 in the

118 SH high-latitude MLT region using MRs located in Antarctica. Plus, we carry out

119 numerical simulations using the Specified Dynamics version of the Whole Atmosphere

120 Community Climate Model (SD-WACCM) nudged towards MERRA-2 reanalysis data

121 in order to elucidate the observed Q10DW-W1 and its amplification mechanism.

122 Section 2 describes two MRs located in the Davis station (68.6°S, 77.9°E) and King

123 Sejong Station (KSS; 62.2°S, 58.8°W) and how we obtain Q10DW-W1 from the

124 observations. Also, the SD-WACCM experiments and Microwave Limb Sounder

125 (MLS) data used for validation are described in Section 2. Results are presented in

126 Section 3. In Section 3.1, we show seasonal variation of observed and modeled

127 Q10DW-W1 in the SH high-latitude MLT region. The amplification mechanism of

128 Q10DW is discussed in Section 3.2. Q10DW activities from SD-WACCM simulations

129 are demonstrated in Section 3.3. In Section 4, the results are summarized, and their

130 implications are discussed.

131

2. Data and Method

2.1 Meteor Radars

134   In this study, we use two MRs located in the Davis station (68.6°S, 77.9°E) and

135 King Sejong Station (KSS; 62.2°S, 58.8°W), Antarctica from 2012 to 2016. The

136 operating frequencies of both Davis and KSS MRs are 33.2 MHz and the peak powers

137 are 6.8 kW and 12 kW, respectively. Details of the operation parameters of Davis and

138 KSS are summarized in Holdsworth et al. (2008) and Lee et al. (2018), respectively. A

139 large number of studies has been performed to investigate the PW or tidal activities in

140 the MLT region with a single-station measurements of horizontal winds from an MR

141 (e.g., Eswaraiah et al., 2019; Luo et al., 2021; Wang et al., 2021; Liu et al., 2022; Lee et

142 al., 2021). However, single-station analysis has a limitation in diagnosing the wave

143 propagation direction, and thus most of such studies focused on the timing of

144 occurrence and amplitude variations of wave with a particular periodicity. For detailed

145 analysis of PWs based on the Rossby normal modes, propagation directions and

146 wavenumbers need to be considered. Recently, He et al. (2018) developed a method of

147 estimating wave propagation direction and wavenumber as well as amplitude by

148 adopting Phase Differencing Technique (PDT) to longitudinally separated MR

149 observations based on the method of Walker et al. (2004). Since the longitude

150 difference (λ_Δ) between Davis and KSS is about 137°, it is appropriate for analyzing

151 PWs with zonal wavenumber 1 by applying the PDT. In order to estimate the zonal

152 wavenumber (s), we first make a continuous wavelet transform from the daily-mean

153 Davis and KSS MRs data ($W_{(f,t)}^{Davis}, W_{(f,t)}^{KSS}$), respectively, using the Morlet wavelet

154 function as a mother wavelet function (Torrence and Compo, 1998). Then, the cross

155 wavelet spectrum $C_{(f,t)}$ is derived: $C_{(f,t)} = W_{(f,t)}^{*Davis} W_{(f,t)}^{KSS}$, where * denotes the complex

156 conjugate. Using the phase difference (θ_Δ) obtained from $\theta_\Delta = \text{Arg}(C_{(f,t)})$ at a given

157 frequency and time, we estimate zonal wavenumber (s): $s = (-\theta_\Delta/(2\pi) + C)/\lambda_\Delta$. In

158 this study, we focus on the PW activity with s = 1, and the number of whole wave cycle

159 (C) between two stations is set to be zero (see He et al., 2018 for detailed PDT analysis).

160   Classical wave theory shows that the latitudinal structures of zonal and

161 meridional wind components for Q10DW normal mode from the Laplace tidal equation

162 are antisymmetric and symmetric with respect to the equator, respectively (e.g., Figure 1

163 in Yamazaki and Matthias, 2019). The magnitude of Q10DW-W1 has maxima at the

164 latitude of 25° and poles for zonal and meridional wind components, respectively.

165 Around the latitude of 65°S close to the latitudes of the two MR observation sites, the

166 normalized amplitude of Q10DW-W1 normal mode for the zonal wind is nearly zero,

167 but the normalized normal mode magnitude for the meridional wind is larger than the

168 half of the maximum magnitude for the meridional wind (Yamazaki and Matthias,

169 2019). For this reason, daily-mean meridional wind data from the MRs is used for the

170 Q10DW analysis.

171

172 **2.2 SD-WACCM**

173   In this study, for detailed analysis of the observed Q10DW-W1 activity and its

174 amplitude mechanism, we compare observational results with Q10DW-W1

175 simulated using the Specified Dynamics (SD) version of WACCM version 4 (Marsh et

176 al., 2013). WACCM4 is a high-top (up to the lower thermosphere about 140 km)

177 atmospheric component model of the Community Earth System Model developed at the

178 National Center for Atmospheric Research. WACCM4 employs Community

179 Atmospheric Model (CAM) version 4 physics package. The default horizontal

180 resolution of WACCM4 is 1.9°×2.5° (lat. × long.), and it uses the 88 hybrid sigma

181 vertical levels for the SD mode. Since we focus on the PWs such as Q10DW-W1, daily-

182 mean values from the SD-WACCM are used. In this study, two SD-WACCM

183 experiments with two different nudging depths (EXP60 and EXP75) are performed. In

184 the EXP60 and EXP75, model variables are nudged towards the MERRA-2 reanalysis

185 data from surface to about 60 km in altitude and 75 km, respectively. The MERRA-2

186 reanalysis is produced by assimilating various types of observations into the Goddard

187 Earth Observing System version 6 (GEOS-6) global model (Gelaro et al., 2017). In

188 addition to conventional meteorological observations and operational satellite

189 measurements, the Earth Observing System (EOS) Aura MLS temperature and ozone

190 data are included in the assimilation procedure of the MERRA-2 from 5 hPa (~37 km)

191 up to 0.02 hPa (~75 km) and from 250 hPa (~10 km) to 0.1 hPa (~65 km), respectively

192 (Gelaro et al., 2017; McCormack et al., 2021). There is a divergence damping layer near

193 the top boundary of the GEOS-6 model used for production of the MERRA-2 reanalysis

194 (Fujiwara et al., 2017). The divergence damping is often used to effectively and

195 selectively remove high-frequency (noisy) gravity waves keeping the large-scale

196 circulation and PWs structure less changed (Jablonowski and Williamson, 2011). As a

197 result, MERRA-2 reanalysis can reflect the large-scale MLT variabilities (e.g.,

198 McCormack et al., 2021; Harvey et al., 2021). As suggested by Brakebusch et al.

199 (2013), nudging coefficients for EXP60 and EXP75 are 0.01 s^{-1} below the altitudes of

200 50 km and 65 km, respectively, and they linearly decrease and become zero above the

201 altitudes of 60 km and 75 km, respectively.

202   WACCM simulation requires the data of sea surface temperature, sea ice

203 fraction, solar and geomagnetic indices, and ionization rate by energetic particle

204 precipitation (EPP) for the time period of simulations. The sea surface temperature and

205 sea ice fraction data are produced by the NOAA Optimum Interpolation (Reynolds et

206 al., 2002). The solar and geomagnetic indices are obtained from NASA GSFC/SPDF

207 OMNIWeb interface (https://omniweb.gsfc.nasa.gov/ow.html). The EPP ionization rate

208 is provided by the CCMI reference-C2 data for the period of 1960–2100 (Eyring et al.,

209 2013). Regarding MLT dynamics, effects of gravity wave drag (GWD) are crucial.

210 WACCM includes a suite of GWD parameterizations (Richter et al., 2010) for effects of

211 unresolved GW momentum transfer from orography (McFarlane, 1987), deep

212 convection (Beres et al., 2005), and frontal activity (Charron and Manzini, 2002). SD-

213 WACCM simulations start from January 1, 2011 and end at the end of 2016. First one-

214 year results are discarded as a spin-up, and results for 2012–2016 are compared with

215 MR observations.

216

217 **2.3 MLS**

218   For validation of Q10DW-W1 estimates obtained from MR observations, we

219 derive the geostrophic winds from geopotential height (GPH) data (version 5.1 product)

220 measured using MLS onboard the NASA's EOS Aura satellite (Schwartz et al., 2008).

221 Geostrophic wind components are computed following Matthias and Ern (2018). The

222   Aura satellite launched on July 2004 is in a sun-synchronous orbit with an altitude of

223   705 km. Spatial coverage of MLS instrument is from 82°S to 82°N with a 165 km

224   resolution along the track. The sun-synchronous orbit of Aura satellite can provide a

225   global coverage data per day with about 15 orbits. The global coverage of GPH is

226   produced using daily mean values in 5°×5° (lat. × long.) grids. In this process, GPH

227   data is filtered on the basis of the recommended precision, status, quality, and

228   convergence thresholds of Version 5.0 Level 2 and 3 data quality and description

229   document (https://mls.jpl.nasa.gov/data/v5-0_data_quality_document.pdf).

230

231   **3. Results and Discussion**

232   **3.1 Seasonal variation of Q10DW-W1 in the MLT region**

233   The perturbation meridional wind for Q10DW-W1 is symmetric in latitude

234   about the equator as mentioned earlier. Therefore, in order to extract and analyze

235   Q10DW-W1, which is potentially related to the Rossby normal mode in the MLT

236   region, it is necessary to confirm whether the latitudinal structure of Q10DW-W1 has

237   the hemispheric symmetry. Although the KSS and Davis MR observations can provide

238   information about the longitudinal propagation of Q10DW-W1, it is impossible to

239   estimate the latitudinal structure using these radars alone. In this study, the meridional

240   geostrophic winds obtained from the MLS geopotential data are used to confirm the

241   hemispheric symmetry of Q10DW-W1 estimated from MRs. The amplitudes of

242   Q10DW-W1 in the MLS are obtained using the two-dimensional Fast Fourier transform

243   (FFT) of the geostrophic meridional winds averaged over the height range of 80–90 km

244   in time (30-day sliding window) and longitude domain. The time-latitude cross section

245 of the amplitude of Q10DW-W1 derived from the MLS geostrophic meridional wind

246 averaged over the height range of 80–90 km is presented in the Supplement (Fig. S1).

247 Hereafter, the Q10DW denotes westward-propagating quasi-10-day normal mode wave

248 with zonal wavenumber 1 and the hemispheric symmetry, where quasi-10-day

249 periodicity means the periods between 9 and 11 days. Unless the hemispheric symmetry

250 is satisfied, the analyzed westward propagating signals with zonal wavenumber 1 are

251 referred to as quasi-10-day-like oscillations (Q10DOs).
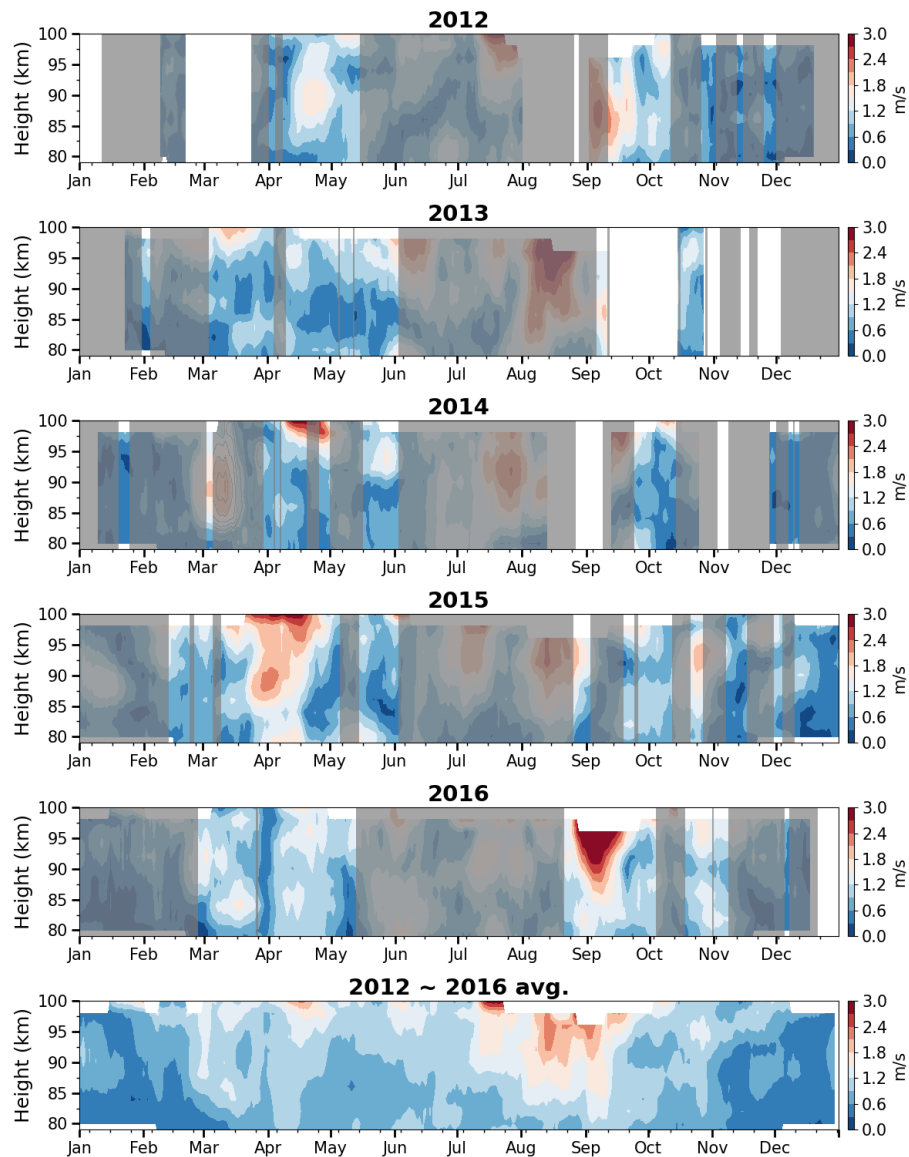
252   Figure 1 shows the time-height distributions of the amplitudes of Q10DWs and

253 Q10DOs derived from the daily-mean meridional winds observed at the Davis and KSS

254 MRs using the PDT method. The regions shaded in gray represent the time periods

255 when the hemispheric symmetry is not found in the MLS results as shown in Fig. S1.

256 The time periods of the hemispheric symmetries are defined by the periods when the

257 amplitudes of the MLS meridional geostrophic winds (vertically averaged over 80–90

258 km) with quasi-10-day periodicity exceed 3.5 m s^{-1} in both 60°N–80°N and 60°S–80°S.

259 The MLS results in solstices are generally shaded in gray (see Fig. S1). This result

260 indicates that Q10DWs in a form of normal modes are found during equinoxes, which is

261 consistent with the results from Forbes and Zhang (2015). Using the periods of the

262 hemispheric symmetry of the Q10DW obtained from the MLS, we identify the normal

263 mode Q10DW from the Davis and KSS MR observations.

264   The 5-yr average (The bottom-most panel of Fig. 1) between 2012 and 2016

265 indicates that the Q10DWs are generally enhanced from late February to April and from

266 late August to September in the altitude range of 82–98 km with the maximum

267 amplitude of 2.6 m s^{-1}. The Q10DWs are usually more amplified in early spring from

268 late August to September with the largest amplitudes around the altitudes of 90–95 km.

269 Large amplitudes are found in winter (July to mid-August), but they are unlikely to

270 represent the normal mode Q10DWs, as it is clear from the gray shading in winter.

271 According to Wang et al. (2021), the nonlinear wave-wave interaction can generate

272 Q10DOs in southern winter. Their Q10DOs are eastward propagating, interacting with

273 stationary PWs with zonal wavenumber 1. Meanwhile, the Q10DWs and Q10DOs (Fig.

274 1) obtained from two MRs using the PDT method are westward propagating.

275 Understanding of the mechanisms of the winter-time westward-propagating Q10DOs is

276 beyond the scope of this study, and it requires continuing researches.

277   For individual years, it is also found that the amplitude of Q10DW is generally

278 large in equinoxes (see panels for each year in Figs. 1 and S1). During March–April

279 (autumn), active Q10DWs are identified, and their amplitudes reach up to ~3 m s^{-1} in

280 2014 and 2015. Particularly, the peak in September (spring) is prominent in 2016. These

281 MR observation results are remarkably consistent with results obtained using satellite

282 geopotential height in the SH high-latitude region (Forbes and Zhang, 2015).

283 Occasionally, large amplitude Q10DWs are observed near the altitude of 98–100 km in

284 equinoxes (e.g., April 2015), but results around 100 km can be less reliable because the

285 number of MR echoes above 96 km is much smaller than that around 90 km (Lee et al.,

286 2022).
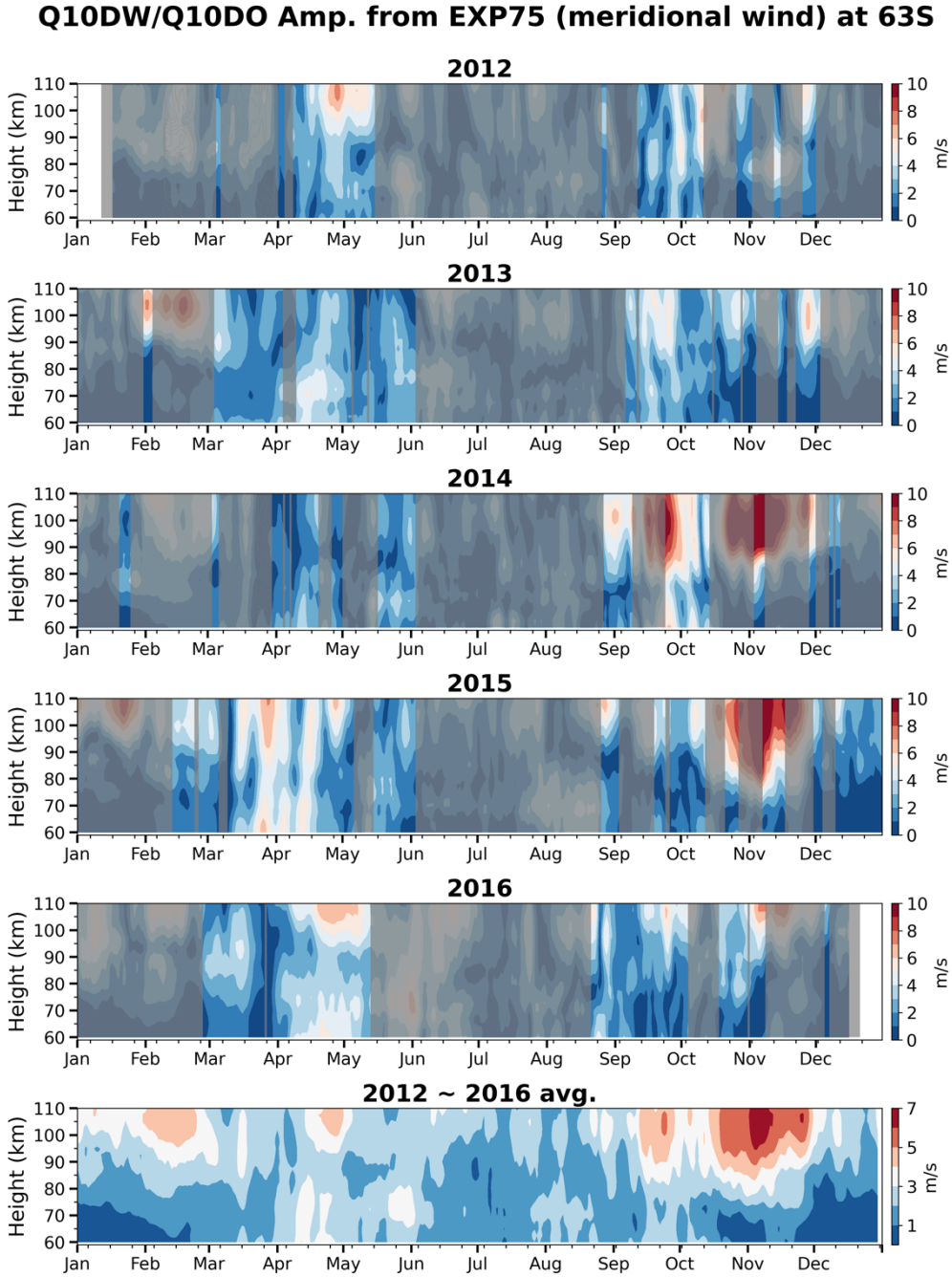
Figure 1. Time-height distributions of the amplitudes of Q10DWs (unshaded region) and Q10DOs (shaded region) derived from meridional winds observed by MRs at Davis (68.6°S, 77.9°E) and KSS (62.2°S, 58.8°W) for 2012–2016. The bottom-most panel shows the 5-yr average from 2012 to 2016. The gray shading represents time periods where the hemispheric symmetry is unclear in the MLS results (see the text for details of the unclearness of symmetry).

294   Figure 2 demonstrates the time-height distributions of the amplitudes of

295   Q10DWs and Q10DOs around the latitude of 63°S in the EXP75 SD-WACCM

296   simulation for the altitude range of 60–110 km for 2012–2016, along with the

297   hemispheric symmetry period obtained from the MLS results. The bottom-most panel of

298   Fig. 2 shows the 5-yr average from 2012 to 2016. The amplitudes are obtained by

299   decomposing the meridional winds obtained from the simulation into westward

300   propagating Fourier modes with zonal wavenumber 1 using the 2D FFT in time (30-day

301   sliding window) and longitude domain around 63°S. From Fig. 2, it is clear that the

302   seasonal variations of Q10DW amplitudes obtained from the simulation have year-to-

303   year variations, as in the Q10DW amplitudes derived from the two MRs. However, the

304   Q10DW activities observed from the MR observations are generally larger than those in

305   the EXP75 simulation (see Fig. 1).

306   The 5-yr average in Fig. 2 shows that there are four main time periods

307   (February, April, September, November) when the modeled Q10DWs and Q10DOs are

308   active in the EXP75. The time periods of April and September are consistent with the

309   MR observations in terms of Q10DW amplitudes and the hemispheric symmetry

310   obtained from the MLS, but the other periods are not. The active signals simulated in

311   February and November do not appear to be normal mode Q10DWs because the

312   hemispheric symmetry is not seen in the MLS data during February and November. For

313   a more comprehensive understanding of the Q10DOs in the EXP75 during February and

314   November, we will discuss in more detail later in Section 3.3 by comparing between the

315   EXP75 and EXP60.

Figure 2. Time-height distributions of the amplitudes of Q10DWs (unshaded region) and Q10DOs (shaded region) around 63°S for 2012–2016 in the EXP75. The bottom-most panel shows the 5-yr average between 2012 and 2016. The gray shaded areas represent periods where the hemispheric symmetry is not observed in the MLS results.

16

321   Figure 3 shows time series of the normalized amplitudes of Q10DWs and

322   Q10DOs obtained from the MR observations (black) and EXP75 simulation (blue).

323   Normalization is carried out by averaging the amplitudes in the altitude range between

324   80 and 100 km and dividing the 5-yr averaged values by the respective maximum

325   values in the same altitude range. We select the dates when (i) the amplitudes obtained

326   from both MRs and EXP75 exceed their respective 5-yr mean values, (ii) their

327   correlation is relatively large (> 0.6), and (iii) the hemispheric symmetry occurs in the

328   MLS results. The correlation coefficients are computed for sliding 7-day windows with

329   1-day step. The dates when the three criteria are satisfied are represented by yellow

330   boxes on abscissa in Fig. 3. The total number of the dates when the Q10DW was

331   substantially active in both observations and model (EXP75) is 46. Using EXP75 results

332   on the selected dates, the amplification mechanisms of the observed Q10DW will be

333   discussed.

Normalized amplitude of Q10DW/Q10DO at 63S [80-100 km]
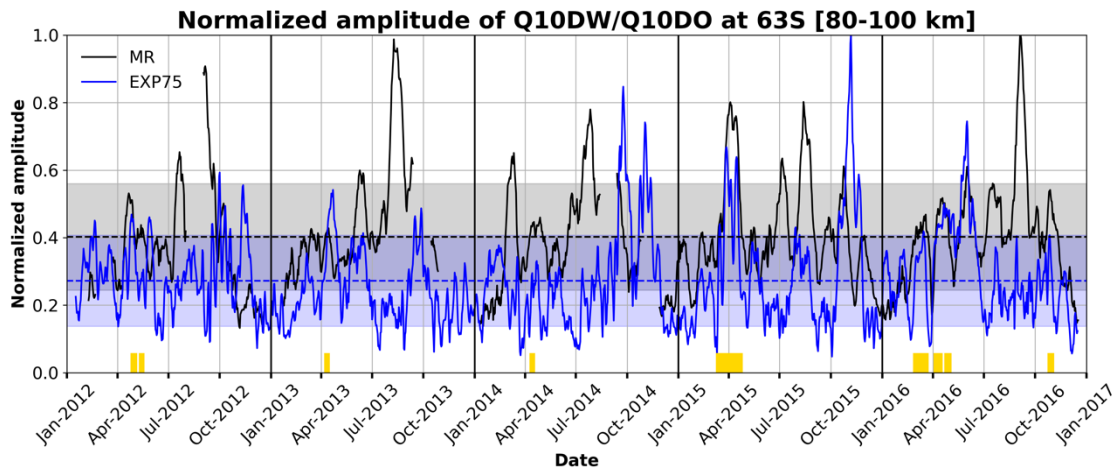
334

335 **Figure 3.** Time series of normalized amplitudes of Q10DW/Q10DOs from the

336 observations (black line) and EXP75 simulation (blue line). The dashed lines and

337 shaded areas represent the mean and standard deviation of normalized amplitude of

338 Q10DW/Q10DOs from the observations (black) and EXP75 (blue), respectively.

339 Yellow boxes on abscissa indicate the dates when the normalized amplitudes from both

340 MRs and EXP75 can be considered to be due to the normal mode Q10DWs.

3.2 Amplification mechanisms of Q10DW

The amplitude of upward propagating PWs grows with height when their vertical propagation is allowed, but it can decrease with height in the evanescent region where the square of refractive index n^2 becomes negative. Regions of negative n^2 are often accompanied by regions of the negative latitudinal gradient of zonal-mean potential vorticity ($\bar{q}_\phi$), where $\bar{q}$ is the zonal-mean quasi-geostrophic potential vorticity (QGPV), the overbar denotes zonal averaging, ϕ is the latitude, and the subscript ϕ denotes the partial derivative in the latitudinal direction. In the regions of negative $\bar{q}_\phi$, the barotropic and baroclinic instabilities can occur (Matsuno, 1970), and it is known that PWs can amplify extracting energy from the mean flow while they pass through the instability regions (Meyer and Forbes, 1997; Cohen et al., 2013). If PWs somehow reach their critical lines within an instability region, it is possible for these PWs to tunnel through the critical lines (Rhodes et al., 2021). In case that the evanescent region is thin enough, and the PWs can reach their critical lines, it is also possible for the overreflection to take place, resulting in the amplified PWs and the propagation of the amplified PWs out of the overreflection region (Lindzen et al., 1980; Rhodes et al., 2021).

Another possible way of modulating PWs is their excitation by the nonconservative GW forcing (Song et al., 2020). Nonconservative GWD forcing (NCGWD; Z') can generate PWs as it is clearly seen from the perturbation QGPV equation given in the form of wave action conservation equation (1) when diabatic forcing is ignored in Z' [see Andrews et al. (1987) and Palmer (1982) for details]:

364 $$\frac{\partial A}{\partial t} + \nabla \cdot \mathbf{F} = \rho_0 \overline{Z' q'_{(M)}}/(\bar{q}_\phi/a),$$ (1)

365

366 where a is the earth's mean radius; ρ_0 is the reference density given as an exponentially

367 decreasing function of log-pressure height z; the prime denotes the perturbation from the

368 respective zonal mean; A, defined below using $q'_{(M)}$, is the wave-activity density in the

369 spherical QG system; $q'_{(M)}$ is the perturbation of modified QGPV, modified to consider

370 the planetary vorticity advection by the isallobaric meridional wind in spherical geometry

371 (Matsuno, 1970; Palmer, 1982); Z' is the curl of the horizontal GWD perturbation; $\nabla \cdot \mathbf{F}$

372 is the divergence of Eliassen-Palm (EP) flux ($\mathbf{F}$), and the flux $\mathbf{F}$ is considered to be the

373 wave-activity flux given by $\mathbf{F} = \mathbf{c}_g A$ in the QG framework, where $\mathbf{c}_g$ is the group velocity

374 in the latitude-height domain.

375   In (1), the wave-activity density A and the modified QGPV perturbation $q'_{(M)}$ are

376 given in spherical geometry (Palmer, 1982), respectively, as follows:

377

378 $$A = a \cos\phi \, \frac{1}{2} \rho_0 \frac{\overline{q'^2_{(M)}}}{\bar{q}_\phi/a},$$ (2)

379 $$q'_{(M)} = \frac{v'_\lambda}{a\cos\phi} - \frac{f}{a\cos\phi}\left(\frac{u'\cos\phi}{f}\right)_\phi + \frac{f}{\rho_0}\left(\rho_0\frac{\theta'}{\bar{\theta}_z}\right)_z,$$ (3)

380

381 where u and v are zonal and meridional wind components, respectively; λ is the

382 longitude; f is the Coriolis parameter; θ is the potential temperature. The subscript λ and

383 z mean the partial derivatives in longitude and vertical directions, respectively.

20

384   For understanding of amplification of PWs around the instability regions, the

385   barotropic and baroclinic instability regions are determined by the negative sign of $\bar{q}_\phi$

386   (Andrews et al. 1987) given by:

387

388    $\bar{q}_\phi = 2\Omega \cos\phi - \left[\frac{(\bar{u}\cos\phi)_\phi}{a\cos\phi}\right]_\phi - \frac{a}{\rho_0}\left(\frac{\rho_0 f^2}{N^2}\bar{u}_z\right)_z$,   (4)

389

390   where Ω is the earth's rotation rate and N is the buoyancy frequency. The negative sign

391   of $\bar{q}_\phi$ is a necessary condition of the barotropic and baroclinic instabilities. The second

392   (with negative sign) and third (with negative sign) terms on the right-hand side of (4)

393   represent the meridional and vertical curvatures of the zonal-mean zonal wind,

394   respectively. If the second or third term is dominant, $\bar{q}_\phi$ can become negative, and the

395   instabilities can take place.

396   The square of refractive index n^2 is used to analyze the propagation

397   characteristics of PWs and depends on the mean QGPV gradient as follows:

398

399    $n^2 = \frac{\bar{q}_\phi}{a(\bar{u}-c)} - \frac{s^2}{a^2\cos^2\phi} - \frac{f^2}{4N^2H^2}$,   (5)

400

401   where c is the zonal phase speed of single PW (i.e., $c = 2\pi a \cos\phi /(s\tau)$; s is the zonal

402   wavenumber, and τ is the wave period), and the constant scale height H is set equal to 7

403   km. The propagation of PWs is possible in regions of positive n^2. On the other hand,

404   PWs can be reflected or be evanescent in the region where $n^2 < 0$ (Matsuno, 1970).

21

405   In order to analyze the wave propagation and wave activity for the selected dates

406 for Q10DWs (or Q10DOs) found in MRs and model simulations, we use the EP flux as

407 diagnostic tools, derived in the Transformed Eulerian-Mean framework for the spherical

408 QG system (Palmer, 1982; Andrews et al., 1987). In the spherical geometry, the

409 meridional $[F^{(\phi)}]$ and vertical $[F^{(z)}]$ components of the EP flux $\mathbf{F} \equiv [0, F^{(\phi)}, F^{(z)}]$ are

410 given by

411

412 $F^{(\phi)} = -\rho_0 a \cos\phi \overline{u'v'}$,   (6)

413 $F^{(z)} = \rho_0 a \cos\phi\, f\, \overline{v'\theta'}/\bar{\theta}_z$,   (7)

414

415   Figure 4 shows the EP flux $\mathbf{F}$ and wave activity density normalized by $\rho_0\, a\cos\phi$

416 for Q10DWs in the EXP75. The propagation inhibition region ($n^2 < 0$) and the

417 contours of zonal-mean zonal wind are overplotted. Thick green and black lines indicate

418 the regions of $\bar{q}_\phi = 0$ and of critical lines for Q10DWs, respectively. The critical lines

419 are plotted by computing the zonal phase speed (c) of Q10DW: $c = 2\pi a \cos\phi\,/(s\tau)$,

420 where $s = 1$ and $\tau = 10$ day. The wave-activity density is shaded in blue and red

421 depending on its sign [sgn(A)]. For the EP flux vector, $\mathbf{F}/\mathrm{sgn}(A)\ (= \mathbf{c}_g|A|)$, rather than

422 $\mathbf{F}$ itself $(= \mathbf{c}_g A)$, is plotted such that the EP flux can always be parallel to the local

423 group velocity of Q10DWs regardless of the instability regions where $\bar{q}_\phi < 0$ and thus

424 $A < 0$. For better illustration of the EP flux in the atmosphere where its density

425 decreases exponentially with height, the meridional and vertical components of EP flux

426 are scaled by $(p_s/p)^{0.85}[F^{(\phi)}/(a\pi), F^{(z)}/(3 \times 10^5)]$ (Edmon et al., 1980; Gan et al.,

427 2018), where p_s and p are the surface and atmospheric pressures, respectively.

428   For Fig. 4, we select the four dates of (a) 30 April 2012, (b) 11 April 2013, (c) 6

429 April 2015, and (d) 29 October 2016 when the three criteria mentioned in Fig. 3 are

430 satisfied (see yellow boxes in Fig. 3). That is, the normalized amplitudes of Q10DWs

431 from both MRs and EXP75 are larger than its average, the correlation coefficient is

432 larger than 0.6, and the hemispheric symmetry is found in the MLS results. The 30

433 April 2012 case (Fig. 4a) shows that the stratospheric jet is located around (40°S–60°S,

434 55 km) in the latitude-height domain and that there is a predominant branch of upward

435 and equatorward Q10DW EP flux vectors across the center of the stratospheric jet. In

436 the high-latitude mesosphere, there are two regions where both the large-scale

437 instability ($\bar{q}_\phi < 0$) and evanescence ($n^2 < 0$) take place, and they are located in

438 (55°S–65°S, 60–85 km) and (65°S–80°S, 70–110 km), respectively. Along the

439 instability boundaries (green lines), large positive or negative Q10DW activities are

440 found. Divergent EP flux vectors in the meridional direction are clearly seen around the

441 instability region located at (53°S, 65–75 km), which implies the excitation of Q10DWs

442 in association with the instability. In the region of MR observations (60°S–65°S, 85–

443 100 km), substantially amplified Q10DW activity appears, and the equatorward

444 Q10DW EP flux towards the MR sites is found over the amplified Q10DW activity.

445   Figure 4b demonstrates the case of 11 April 2013. One major branch of Q10DW

446 EP flux vectors (Fig. 4b) originates from the stratospheric jet located at (55°S–60°S,

447 45–60 km). In the southern and upper side of the stratospheric jet, the instability and

448 evanescent region extends from 45 km to 70 km height in the latitude of 50°S–75°S.

449   Above the instability region, distinct region of strong wave activity is found around

450   (50°S–65°S, 65–90 km), and this region is partially overlapped by the MR observation

451   region. Around this region, the Q10DW EP flux is directed downward and poleward

452   inside of the instability region (within green line). The Q10DW EP flux is directed

453   upward and equatorward outside and above the instability region. This diverging pattern

454   of EP flux around the instability region also shows the possibility of the excitation of

455   Q10DW in association with the instability.

456   For 6 April 2015 case (Fig. 4c), the structure of wave-activity density and

457   instability regions are similar to the 30 April 2012 case (Fig. 4a). The instability and

458   evanescent regions occur around (60°S–80°S, 70–100 km). Along the instability

459   boundaries, there are strong positive and negative wave-activity densities, and this

460   region of strong wave activities includes the MR observation region. Again, the

461   divergence of Q10DW fluxes appears in the upper part of the instability region around

462   (60°S–70°S, 80–100 km). The Q10DW propagates upward and equatorward outside of

463   the instability region and downward inside of the instability region, as in the other dates

464   shown in Figs. 4a and 4b. Unlike the other events, the propagation of Q10DW is

465   poleward in the stratosphere (30–60 km altitude). This result is consistent with Qin et al.

466   (2022). They reported that the meridional component of EP flux extends from the

467   stratosphere in the NH across the equator to the SH stratosphere during the westerly

468   phase of QBO in the middle stratosphere and during the westerly phase of the semi-

469   annual oscillation in the upper stratosphere.

470   In 29 October 2016 case (Figure 4d), the center of stratospheric jet is located

471   around (60°S–70°S, 20–30 km). Above the stratospheric jet, the eastward wind turns

472 westward around the altitude of 60 km. Within the region of westward wind, the

473 instability and evanescent regions are found. In addition, the critical lines exist inside

474 the instability region. The overreflection or transmission process can take place near the

475 critical lines as we mentioned. Notably, the significantly large positive and negative

476 wave-activity density regions are found around (45°S–70°S, 60–90 km) near the

477 instability boundaries, and these regions are partially overlapped by the MR observation

478 region. This result suggests that the observed amplification of Q10DW may be

479 attributed to the overreflection process. The EP flux of Q10DW predominantly

480 propagates upward and equatorward away from the strong wave-activity region around

481 (60°S, 60–70 km) with weak poleward propagation of Q10DW towards the instability

482 region across the critical lines.

483   For all the cases shown in Fig. 4, the results indicate that a distinct strong wave-

484 activity density region is located within the area observed by the MRs (around 60°S–

485 70°S and 80–100 km in height), associated with the large-scale instability region.

486 Considering the wave-activity density A is directly proportional and inverse

487 proportional to the $\overline{q'^2}$ and $\bar{q}_\phi$, respectively, it can be thought that the small $\bar{q}_\phi$

488 contributes the large magnitude of A near the instability region. However, we confirm

489 that the large $\overline{q'^2}$ is located around the instability region, leading to the overall large

490 wave-activity density (not shown in here). In addition, the group velocity of the wave is

491 given by $\mathbf{c}_g = \mathbf{F}/A$. For the selected cases (Fig. 4), the EP flux $\mathbf{F}$ in the MR observation

492 region is relatively small, while the magnitude of A is comparatively large. This

493 suggests a small group velocity in this region. These results agree with the study of

494   Thorncroft et al. (1993), which states that during the amplification of baroclinic waves,

495   the group velocity tends to be small.

496   As previously mentioned, Song et al. (2020) proposed that the NCGWD can

497   generate PWs. In addition, Forbes and Zhang (2015) suggested that the dissipation of

498   gravity waves filtered by the Q10DW wind field can generate a secondary Q10DW by

499   momentum deposition. In this regard, the both parameterized GWs and resolved GWs

500   ($s \geq 20$) could also play a role in generating Q10DW. To verify the contribution of

501   NCGWD, we analyze linearized disturbance QGPV equation (Andrews et al., 1987) for

502   the 4 cases shown in Fig. 4. Our analysis shows that the contribution of both NCGWD

503   and resolved GW for the Q10DW is negligible in the MLT region (see Fig. S3 in the

504   Supplement).

505   These results indicate that the large amplitudes of Q10DW observed in the SH

506   high-latitude region by the Davis and KSS MRs can originate from the high-latitude

507   stratosphere-mesosphere region, where the barotropic/baroclinic instability or

508   overreflection near the critical layer occur.
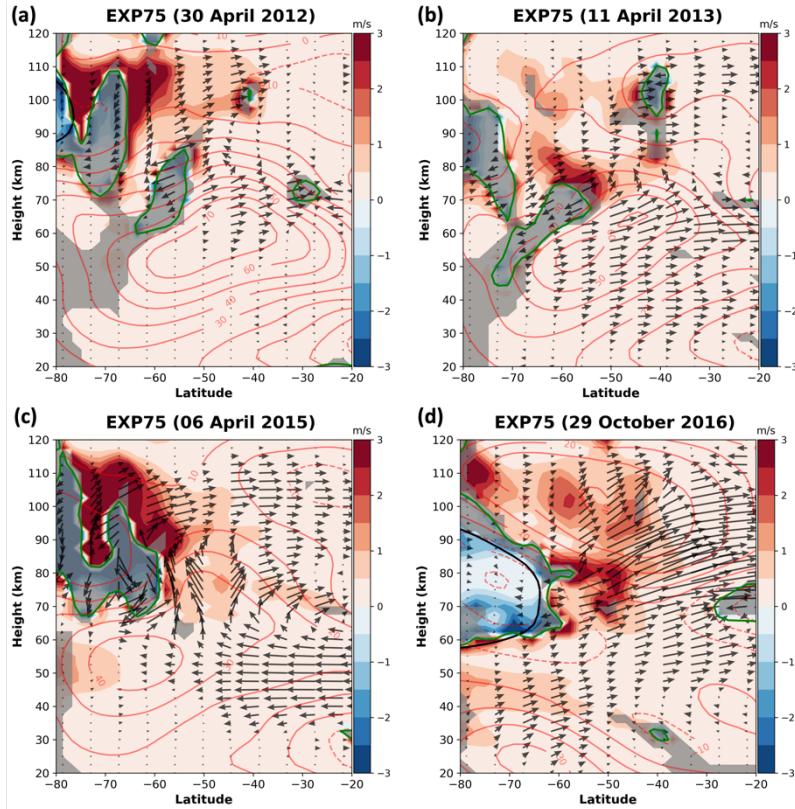
Figure 4. EP flux parallel to local group velocity [F/sgn(A)] and normalized wave

activity density [$A\,(\rho_0 a \cos \phi)^{-1}$ given in the unit of m s^{-1}] for the Q10DWs in the

EXP75 on (a) 30 April 2012, (b) 11 April 2013, (c) 6 April 2015, and (d) 29 October

2016. The activity density A is shaded in blue and red depending on its sign. The

boundaries of the instability regions ($\bar{q}_\phi = 0$, green lines), the negative n^2 regions (grey

shading), and the red contours for zonal-mean zonal wind are overplotted. For eastward

(westward) zonal-mean zonal wind, contours are plotted in solid (dashed) lines, and

contour interval is 10 m s^{-1}.

**3.3 Comparison of Q10DO between SD-WACCM simulations**

This section compares the Q10DOs around the mesospheric instability regions

in the two SD-WACCM simulations (EXP75 and EXP60) for February and November.

521 February and November are chosen because the amplitudes of modeled Q10DOs are

522 substantial. The magnitude of Q10DO in the EXP75 is generally smaller than that in the

523 EXP60, which is more comparable to the MR and MLS observations in which both

524 Q10DWs and Q10DOs are weak (see Figs. S1 and S2 in the Supplement). Note that

525 more realistic meteorological fields are nudged throughout the mesosphere in the

526 EXP75. In this section, comparison between EXP75 and EXP60 for February and

527 November is carried out to reveal mechanisms behind weak Q10DOs in the EXP75.

528   Figure 5 demonstrates the properties of Q10DO and background atmospheric

529 conditions (as shown in Fig. 4) for 5 February 2013 and 16 November 2016 when the

530 Q10DO activity is found to be large in both simulations. The left and right panels of

531 Fig. 5 are the results from the EXP75 and EXP60, respectively. In Fig. 5, it is clear that

532 the strong wave-activity density for Q10DO arise in polar regions above the altitude of

533 70 km in the EXP60, and the magnitude of the EP fluxes in the EXP60 is much larger

534 than that in EXP75. In addition, in 5 February 2013 for the EXP60 (Fig. 5b), a

535 substantially strong wave-activity density region is located in the mid-latitude

536 mesospheric region as well. Around the strong wave-activity regions in the polar upper

537 mesosphere, it is seen that the EP fluxes of Q10DWs are divergent. In addition, the

538 distinct wave-activity density of Q10DO regions in the EXP60 occur along the

539 instability regions and critical lines around (50°S–70°S, 70–110 km) and (20°S–40°S,

540 65–80 km). On the other hand, the wave-activity density of Q10DO in the EXP75 (Fig.

541 5a and 5c) is located at relatively higher altitudes (80–100 km), and the strength of

542 Q10DO EP flux and wave-activity density are weaker than EXP60. Moreover, the

543 negative EP flux divergence (EPFD) is much larger in the EXP60 than in the EXP75

544 above the altitude of 80 km (not shown in here).

545   Our analysis reveals that the larger wave-activity density and EP fluxes in the

546   EXP60 along the large-scale instability region in the polar upper mesosphere compared

547   to the EXP75. This indicates that the stronger large-scale instability in the EXP60 can

548   amplify Q10DO activities, which is consistent with the analysis result that the

549   barotropic and baroclinic instabilities can be the major sources of the amplification of

550   traveling PWs (Harvey et al., 2019).
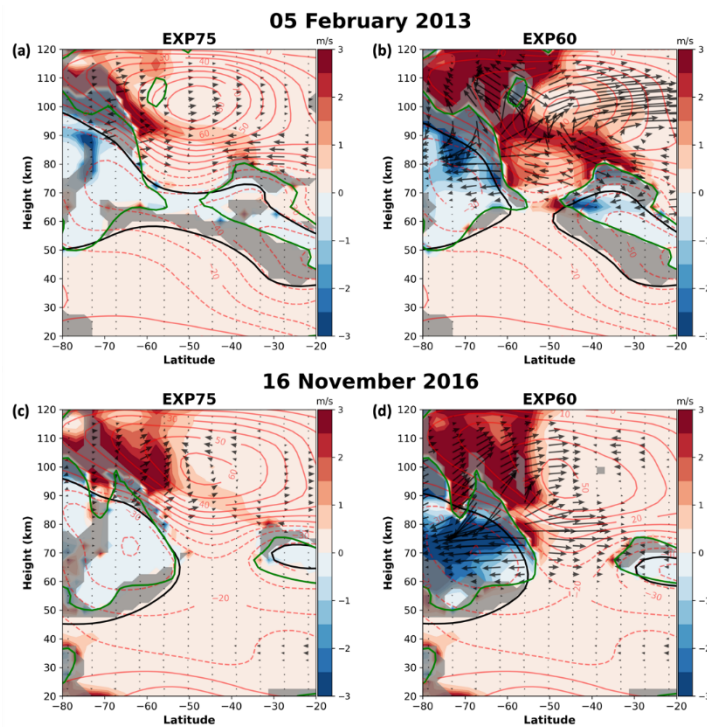
551

552   **Figure 5.** Same as Fig. 4 but for (a and b) 5 February 2013 and (c and d) 15 November

553   2016. The left and right columns represent the results from EXP75 and EXP60,

554   respectively.

555   Figure 6 shows the $\bar{q}_\phi$ (normalized by Ω) for 5 February 2013 and 16 November

556   2016 from the EXP75 (blue), EXP60 (red), and MLS (black). The normalization makes

557    $\bar{q}_\phi$ dimensionless. The $\bar{q}_\phi/\Omega$ from MLS is derived in the quasi-geostrophic framework

558   (Andrews et al., 1987) and it is included as a reference for validation. The $\bar{q}_\phi/\Omega$ is

559   averaged between the latitudes of 65°S-80°S where the wave-activity density is strong

560   and large negative $\bar{q}_\phi$ is found in Fig. 5. It is seen that the vertical profiles of $\bar{q}_\phi/\Omega$

561   from the EXP75 and MLS have somewhat small negative values and they are generally

562   similar below the altitude of 75 km, although the difference gradually increase above

563   the altitude of 75 km. On the other hand, large discrepancies are shown between EXP75

564   and EXP60 in the altitudes between 60–80 km. In the EXP60, $\bar{q}_\phi/\Omega$ has much larger

565   negative values, which suggest the relatively stronger barotropic or baroclinic instability

566   in the EXP60 and the amplification of the Q10DO in the mid-to-upper mesosphere in

567   association with the stronger instability in the EXP60.
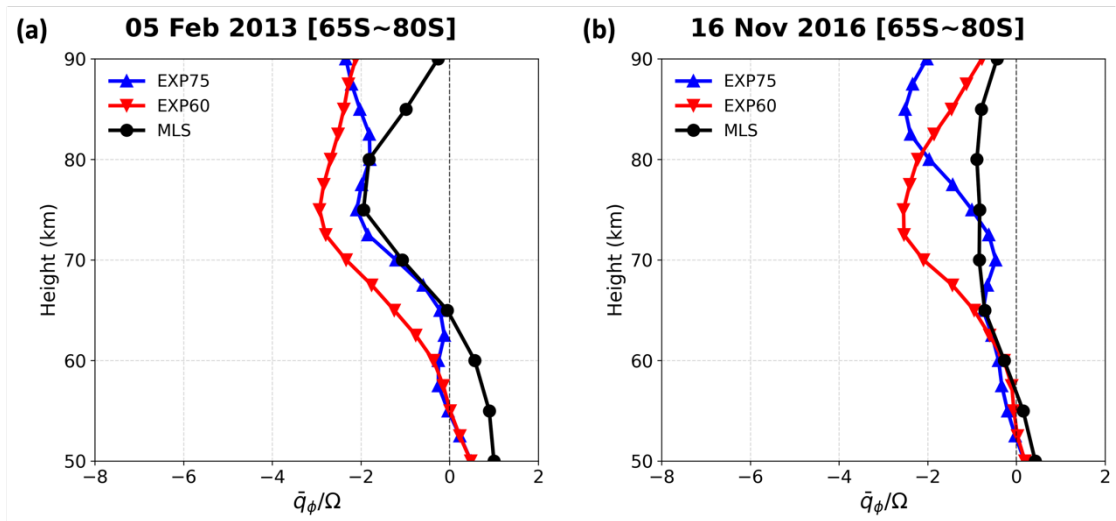
568

569   **Figure 6.** $\bar{q}_\phi$ (normalized by Ω) averaged over 65°S–85°S for (a) 5 February 2013 and

570   (b) 16 November 2016 from the EXP75 (blue), EXP60 (red), and MLS (black).

571   The negative $\bar{q}_\phi$ can be induced by latitudinal and vertical curvatures of zonal-

572   mean zonal wind that correspond to the second and third terms (with negative signs) in

573   the right side of (4), respectively. Figure 7 shows the second (top panels) and third

574 (bottom panels) terms, respectively, for 5 February 2013. The differences shown in

575 Figs. 7c and 7f indicate that the larger negative $\bar{q}_\phi$ is located in the lower altitudes in the

576 EXP60 than in EXP75, inducing the larger instability at 65–75 km in height around

577 70°S–80°S in the EXP60, which is consistent with Fig. 6. Note that the positive

578 differences seen at about 65–75 km in the high-latitude regions in Figs. 7c and 7f mean

579 the larger negative $\bar{q}_\phi$ in the EXP60. Also, it is clear that both vertical and horizontal

580 shear contribute the stronger barotropic/baroclinic instability in the EXP60 in the mid-

581 to-upper mesosphere, as shown in Figs. 7a-b and 7d-e. This analysis demonstrates the

582 mesospheric dynamics specified by the MERRA-2 data up to the altitude of 75 km

583 reduces the large-scale instability in the mid-to-upper mesosphere in the EXP75. This is

584 consistent with Sassi et al. (2021) proposed the absence of specification of middle

585 atmosphere dynamics induce the instability in summer mesospheric westward jet,

586 leading large traveling PWs.

587   The wind structure in the MLT region is mainly driven by momentum

588 deposition from PWs and GWs. Harvey et al. (2019) reported that GWs can change

589 significantly the vertical shears, leading enhanced instability and larger traveling PWs in

590 the mesospheric region based on the satellite observations and SD-WACCM

591 simulations. GW forcing is one of the main factors to maintain the necessary conditions

592 of barotropic/baroclinic instability in the modeled mesosphere (Sato et al., 2018).

593 Therefore, in order to better understand the mechanisms underlying the discrepancies in

594 zonal wind fields and the resulting instability in the model, it is important to examine

595 the contribution of resolved wave forcing (EPFD) and GWD forcing on the zonal wind

596 structure in the mesosphere.
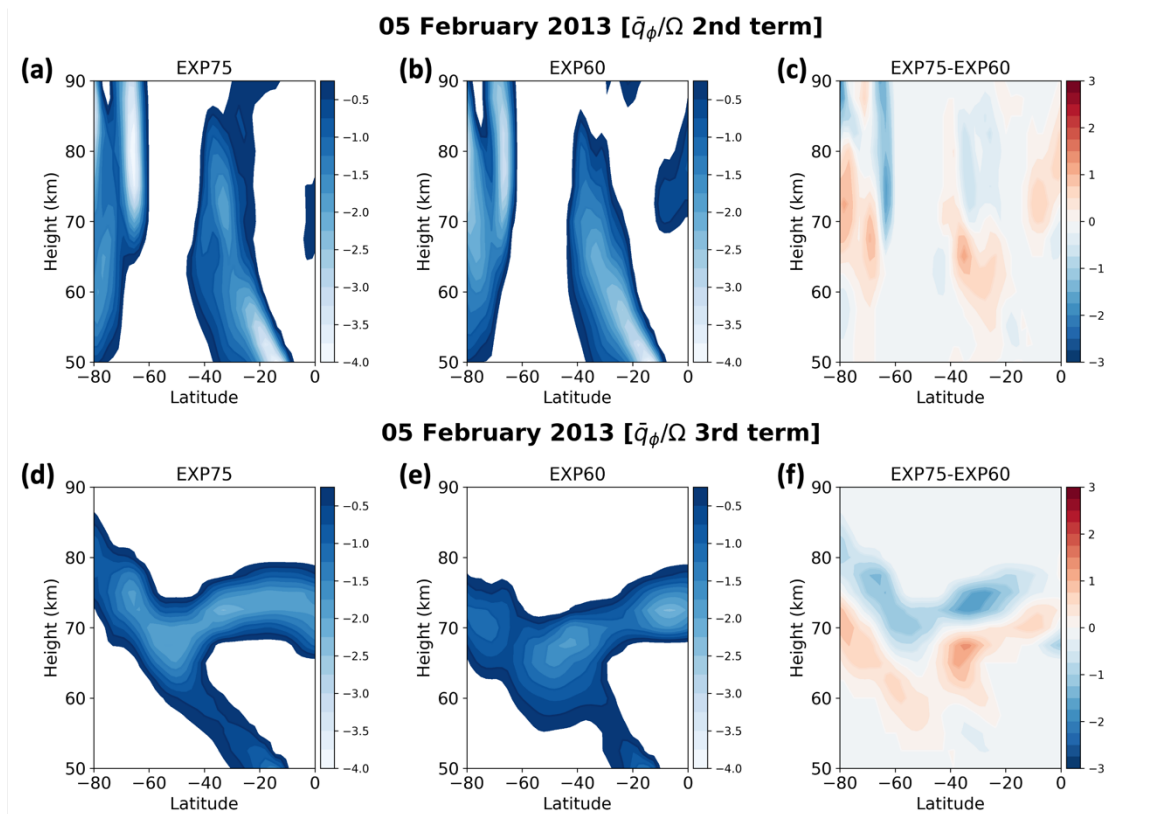
Figure 7. Contributions of (top) the meridional variation of the zonally-averaged mean flow and (bottom) its vertical variation to the instability condition (negative $\bar{q}_\phi$) shown in (2), respectively, for 5 February 2013. Panels in each column present the results from (a and d) the EXP75, (b and e) the EXP60, and (c and f) difference between EXP75 and EXP60, respectively. Only negative values are plotted except for two panels for difference.
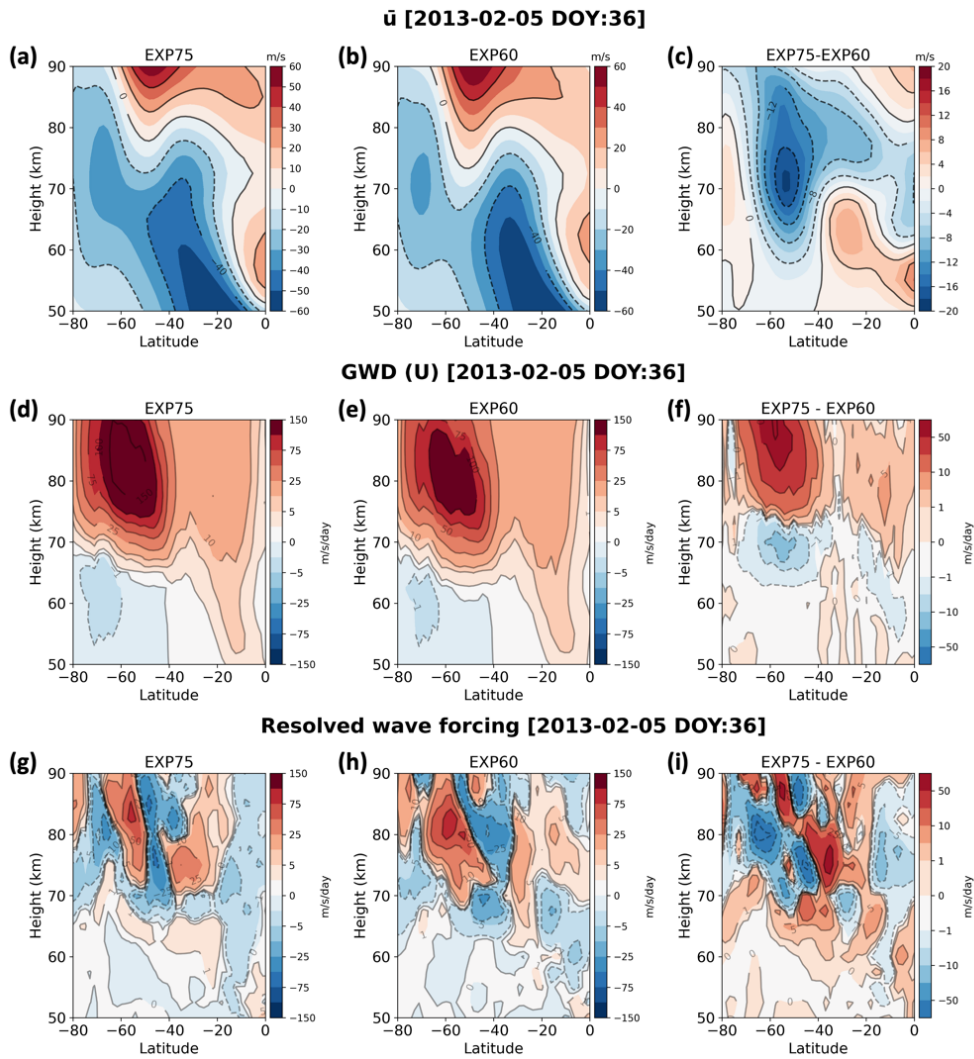
Figure 8 shows the latitude-height distributions of zonal-mean zonal wind, zonal component of GWD and resolved wave forcing (EPFD) in 5 February 2013 for the EXP75, the EXP60, and the difference between EXP75 and EXP60 (EXP75–EXP60). The zonal-mean zonal wind, zonal component of GWD, and resolved wave forcing (EPFD) are calculated through the 21-day averaging (central date ± 10 days). For GWD, the orographic and nonorographic values are added. In Figs. 8a–b, zero-wind lines are

610 located around 80 km height in the SH mid-latitude region, indicating the reversal of the

611 zonal-mean zonal wind due to the eastward momentum forcing from the GWs and

612 resolved waves. It is clear that the zero-wind line in the EXP60 is located at lower

613 altitudes by about 5 km compared to the EXP75, which means that eastward GWD and

614 eastward EPFD from the EXP60 can be larger below the altitude of ~80 km than that

615 from EXP75. Indeed, the difference field between EXP75 and EXP60 for GWD (Fig.

616 8f) shows that the eastward GWD from the EXP60 is larger around (60°S, 70 km) than

617 that from EXP75 as indicated by the negative difference field in those regions. In

618 addition, the resolved wave forcing (EP flux divergence) is more eastward above the

619 altitude of 70 km in the mid-to-high latitude regions in the EXP60 than in the EXP75.

620 This result indicates that the eastward resolved wave forcing also contributes more in

621 the mid-to-upper mesosphere in the EXP60, resulting in the zonal-mean zonal wind

622 reversal (westward to eastward wind) in the lower altitude in the EXP60, as shown

623 around 60°S in Fig. 8b.

624   As mentioned before, the amplification or modulation of westward-propagating

625 PWs with zonal wavenumber 1 and a quasi-10-day period due to NCGWD and resolved

626 GW is negligible (Fig. S3 in Supplement), indicating that the amplification of Q10DW

627 or Q10DO is mainly related to the baroclinic/barotropic instability. The stronger

628 instability in the EXP60 around the altitude of 70 km indicates that WACCM simulates

629 a large meridional and vertical variation of zonal winds compared to the observations in

630 the mid-to-upper mesosphere, which is likely due to the stronger eastward GWD and

631 eastward EPFD forcing near 70 km altitude in the EXP60, as shown in Fig. 8. Cohen et

632 al. (2013) reported that parameterized GWs can generate instability that can generate

633 resolved waves of which forcing (i.e., EPFD) can compensate GWD. Our results show

634 that the increased eastward GWD at 70 km altitude generates instability and it leads

635 more Q10DO. The EPFD in the EXP60 gives the more eastward forcing above 70 km

636 enhancing the wind reversal in the mid-to-high latitudes. However, comparison of Figs.

637 8f and 8i indicates that the structures of GWD and EPFD are roughly 90°–180° shifted

638 in the vertical direction, approximately consistent with the compensation between GWD

639 and EPFD. Raising the nudging altitude of MERRA-2 reanalysis data to 75 km from 60

640 km reduces the instability in the mid-to-upper mesosphere, leading to decreased the

641 Q10DO activity in the EXP75. Therefore, we suggest that strong eastward GWD in the

642 mid-to-upper mesosphere in summer need to be alleviated, which can generate more

643 instability in the SH high-latitude mesosphere region that can lead to discrepancy from

644 observations.

Figure 8. Latitude-height distributions of (a–c) zonal-mean zonal wind, (d–f) zonal component of GWD and (g–i) resolved wave forcing (EP flux divergence) in 5 February 2013 for (left) the EXP75, (middle) the EXP60, and (right) difference between EXP75 and EXP60 (EXP75–EXP60).

4. Summary

651

652   In this paper, the seasonal variation and the amplification mechanism of

653 Q10DW during 2012–2016 in the SH high-latitude regions are investigated using two

654 MRs located in Antarctica, and SD-WACCM simulations. Using the phase difference of

655 meridional winds measured by two MRs, we extract westward-propagating Q10DW

656 with zonal wavenumber 1. The seasonal variation of the observed Q10DW shows that

657 the amplitude is strong during equinoxes, which is consistent with previous studies. In

658 order to elucidate the amplification mechanism of Q10DW observed by MRs during

659 equinoxes, two SD-WACCM experiments are carried out using the MERRA-2

660 reanalysis data from surface to ~60 km (EXP60) and ~75 km (EXP75), respectively.

661 The temporal variation of the averaged amplitude of Q10DW in the EXP75 during

662 2012–2016 is in better agreement with the MR observations. Meanwhile, the amplitude

663 of Q10DW in the EXP60 is excessively large compared with the observations. Based on

664 the analysis of meridional gradient of the QGPV and wave-activity density, the Q10DW

665 observed in the SH high-latitude region by the MRs originated in situ around the high-

666 latitude stratosphere-mesosphere region, where the large-scale instability or

667 overreflection near the critical lines occur. The unrealistically large magnitude of

668 Q10DO (quasi-10-day-like oscillations without satisfying the hemispheric symmetry

669 unlike Q10DW) is simulated in the EXP60 during February and November. In order to

670 understand mechanisms of the large amplitude of Q10DO in the EXP60 during the SH

671 summer, we compare the meridional gradient of QGPV from EXP75 and EXP60. The

672 results show that specified dynamics with MERRA-2 reanalysis data mitigate the

673 meridional and vertical variation of zonal winds in the polar mid-to-upper mesosphere

674 in the EXP75, leading reduction in the large-scale instability. On the other hand, the

675 large amplitude of Q10DO in the EXP60 is attributed to the large-scale instability

676 related to the GWD and partially to the EPFD in the polar mid-to-upper mesosphere.

677 The polar mesospheric GWD can lead to strong large-scale instability in the SH high-

678 latitude mesosphere and unrealistically large amplitude of Q10DO in summer. The

679 present study on the amplification mechanism of Q10DW during equinoxes, and the

680 unrealistic Q10DO amplitude in summer provide potential importance of large-scale

681 instability, which can be to a substantial degree caused by parameterized GWD, during

682 summer in the polar mesosphere for numerical models. In this paper, we focus on the

683 Q10DW relating to the large-scale instability and polar mesospheric GWD, but other

684 normal modes of PW will be considered for future studies.

685 **Code and Data availability**

686   The source code of Community Earth System Model 2 (CESM2) developed at

687 the National Center for Atmospheric Research (NCAR) is available at

688 https://www.cesm.ucar.edu/models/cesm2. The atmospheric forcing data for specified

689 dynamics are available from NCAR Research Data Archive (RDA) at

690 https://rda.ucar.edu.

691   The Davis station meteor radar data are available from the Australian Antarctic

692 Data Centre at https://data.aad.gov.au/metadata/records/Davis_33MHz_Meteor_Radar.

693 The King Sejong Station meteor radar data are available from Korea Polar Data Center

694 (KPDC) at https://kpdc.kopri.re.kr. The GPH data from the MLS onboard the NASA's

695 EOS Aura satellite are available from Goddard Earth Science Data and Information

696 Services Center (GES DISC) at https://daac.gsfc.nasa.gov.

Author contributions

WL and ISS designed the study, together with YHK, and wrote the manuscript. WL performed the analysis of the observational (MR and satellite) data in collaboration with ISS. ISS designed the SD-WACCM experiments. WL and ISS carried out the SD-WACCM experiments, ISS and BGS aided in interpreting the analysis of action conservation equation for Rossby waves. All authors discussed the results and contributed to the final manuscript.

Competing interests

The authors declare that they have no conflict of interest.

Acknowledgements

References

Andrews, D. G., Holton, J. R., and Leovy, C. B.: Middle Atmosphere Dynamics, Elsevier, New York, USA, 489 pp., 1987.

Beres, J. H., Garcia, R. R., Boville, B. A., and Sassi, F.: Implementation of a gravity wave source spectrum parameterization dependent on the properties of convection in the

716   Whole Atmosphere Community Climate Model (WACCM), J. Geophys. Res.-Atmos.,

717   110, https://doi.org/10.1029/2004jd005504, 2005.

718   Brakebusch, M., Randall, C. E., Kinnison, D. E., Tilmes, S., Santee, M. L., and

719   Manney, G. L.: Evaluation of Whole Atmosphere Community Climate Model

720   simulations of ozone during Arctic winter 2004–2005, J. Geophys. Res.-Atmos., 118,

721   2673–2688, https://doi.org/10.1002/jgrd.50226, 2013.

722   Chandran, A., Garcia, R. R., Collins, R. L., and Chang, L. C.: Secondary planetary

723   waves in the middle and upper atmosphere following the stratospheric sudden warming

724   event of January 2012, Geophys. Res. Lett., 40, 1861–1867,

725   https://doi.org/10.1002/grl.50373, 2013.

726   Charron, M. and Manzini, E.: Gravity waves from fronts: Parameterization and middle

727   atmosphere response in a general circulation model, J. Atmos. Sci., 59, 923–941,

728   https://doi.org/10.1175/1520-0469(2002)059<;0923:gwffpa>2.0.co;2, 2002.

729   Cohen, N. Y., Gerber, E. P. and Bühler, O.: Compensation between resolved and

730   unresolved wave driving in the stratosphere: Implications for downward control, J.

731   Atmos. Sci., 70, 3780–3798, https://doi.org/10.1175/jas-d-12-0346.1, 2013.

732   Danabasoglu, G., Lamarque, J. -F., Bacmeister, J., Bailey, D. A., DuVivier, A. K.,

733   Edwards, J., Emmons, L. K., Fasullo, J., Garcia, R., Gettelman, A., Hannay, C.,

734   Holland, M. M., Large, W. G., Lauritzen, P. H., Lawrence, D. M., Lenaerts, J. T. M.,

735   Lindsay, K., Lipscomb, W. H., Mills, M. J., Neale, R., Oleson, K. W., Otto-Bliesner, B.,

736   Phillips, A. S., Sacks, W., Tilmes, S., Kampenhout, L., Vertenstein, M., Bertini, A.,

737 Dennis, J., Deser, C., Fischer, C., Fox-Kemper, B., Kay, J. E., Kinnison, D., Kushner, P.

738 J., Larson, V. E., Long, M. C., Mickelson, S., Moore, J. K., Nienhouse, E., Polvani, L.,

739 Rasch, P. J., and Strand, W. G.: The Community Earth System Model Version 2

740 (CESM2), J. Adv. Model. Earth. Sy., 12, https://doi.org/10.1029/2019ms001916, 2020.

741 Day, K. A. and Mitchell, N. J.: The 5-day wave in the Arctic and Antarctic mesosphere

742 and lower thermosphere, J. Geophys. Res.-Atmos., 1984–2012, 115,

743 https://doi.org/10.1029/2009jd012545, 2010.

744 Edmon, H. J., Hoskins, B. J., and McIntyre, M. E.: Eliassen-Palm cross sections for the

745 troposphere, J. Atmos. Sci., 37, 2600–2616, https://doi.org/10.1175/1520-

746 0469(1980)037<;2600:epcsft>2.0.co;2, 1980.

747 Egito, F., Takahashi, H., and Miyoshi, Y.: Effects of the planetary waves on the MLT

748 airglow, Ann. Geophys., 35, 1023–1032, https://doi.org/10.5194/angeo-35-1023-2017,

749 2017.

750 Eswaraiah, S., Kim, Y. H., Hong, J., Kim, J.-H., Ratnam, M. V., Chandran, A., Rao, S.

751 V. B., and Riggin, D.: Mesospheric signatures observed during 2010 minor

752 stratospheric warming at King Sejong Station (62°S, 59°W), J. Atmos. Sol-Terr. Phy.,

753 140, 55–64, https://doi.org/10.1016/j.jastp.2016.02.007, 2016.

754 Eswaraiah, S., Ratnam, M. V., Kim, Y. H., Kumar, K. N., Chalapathi, G. V.,

755 Ramanajaneyulu, L., Lee, J., Prasanth, P. V., Thyagarajan, K., and Rao, S. V. B.:

756 Advanced meteor radar observations of mesospheric dynamics during 2017 minor SSW

757 over the tropical region, Adv. Space. Res., 64, 1940–1947,

758 https://doi.org/10.1016/j.asr.2019.05.039, 2019.

759 Eyring, Veronika, et al.: Overview of IGAC/SPARC Chemistry-Climate Model

760 Initiative (CCMI) community simulations in support of upcoming ozone and climate

761 assessments, SPARC newsletter, 40, 48–66, https://oceanrep.geomar.de/id/eprint/20227,

762 2013.

763 Forbes, J. M. and Zhang, X.: Quasi-10-day wave in the atmosphere, J. Geophys. Res.-

764 Atmos., 120, 11,079–11,089, https://doi.org/10.1002/2015jd023327, 2015.

765 Forbes, J. M. and Zhang, X.: The quasi-6 day wave and its interactions with solar tides,

766 J. Geophys. Res.-Space, 122, 4764–4776, https://doi.org/10.1002/2017ja023954, 2017.

767 Forbes, J. M., Hagan, M. E., Miyahara, S., Vial, F., Manson, A. H., Meek, C. E., and

768 Portnyagin, Y. I.: Quasi 16-day oscillation in the mesosphere and lower thermosphere,

769 J. Geophys. Res.-Atmos., 100, 9149–9163, https://doi.org/10.1029/94jd02157, 1995.

770 Forbes, J. M., Zhang, X., Heelis, R., Stoneback, R., Englert, C. R., Harlander, J. M.,

771 Harding, B. J., Marr, K. D., Makela, J. J., and Immel, T. J.: Atmosphere-Ionosphere (A-

772 I) coupling as viewed by ICON: Day-to-day variability due to planetary wave (PW)-tide

773 interactions, J. Geophys. Res.-Space, 126, https://doi.org/10.1029/2020ja028927, 2021.

774 Fujiwara, M., Wright, J. S., Manney, G. L., Gray, L. J., Anstey, J., Birner, T., Davis, S.,

775 Gerber, E. P., Harvey, V. L., Hegglin, M. I., Homeyer, C. R., Knox, J. A., Krüger, K.,

776 Lambert, A., Long, C. S., Martineau, P., Molod, A., Monge-Sanz, B. M., Santee, M. L.,

777 Tegtmeier, S., Chabrillat, S., Tan, D. G. H., Jackson, D. R., Polavarapu, S., Compo, G.

778 P., Dragani, R., Ebisuzaki, W., Harada, Y., Kobayashi, C., McCarty, W., Onogi, K.,

779 Pawson, S., Simmons, A., Wargan, K., Whitaker, J. S., and Zou, C.-Z.: Introduction to

780 the SPARC Reanalysis Intercomparison Project (S-RIP) and overview of the reanalysis

781 systems, Atmos. Chem. Phys., 17, 1417–1452, https://doi.org/10.5194/acp-17-1417-

782 2017, 2017.

783 Gan, Q., Oberheide, J., and Pedatella, N. M.: Sources, sinks, and propagation

784 characteristics of the quasi 6-day wave and its impact on the residual mean circulation,

785 J. Geophys. Res.-Atmos., 123, 9152–9170, https://doi.org/10.1029/2018jd028553, 2018.

786 Gelaro, R., McCarty, W., Suárez, M. J., Todling, R., Molod, A., Takacs, L., Randles, C.

787 A., Darmenov, A., Bosilovich, M. G., Reichle, R., Wargan, K., Coy, L., Cullather, R.,

788 Draper, C., Akella, S., Buchard, V., Conaty, A., Silva, A. M. da, Gu, W., Kim, G.-K.,

789 Koster, R., Lucchesi, R., Merkova, D., Nielsen, J. E., Partyka, G., Pawson, S., Putman,

790 W., Rienecker, M., Schubert, S. D., Sienkiewicz, M., and Zhao, B.: The Modern-Era

791 Retrospective Analysis for Research and Applications, Version 2 (MERRA-2), J.

792 Climate, 30, 5419–5454, https://doi.org/10.1175/jcli-d-16-0758.1, 2017.

793 Goncharenko, L. P., Harvey, V. L., Greer, K. R., Zhang, S. -R., and Coster, A. J.:

794 Longitudinally dependent low-latitude ionospheric disturbances linked to the Antarctic

795 sudden stratospheric warming of September 2019, J. Geophys. Res.-Space, 125,

796 https://doi.org/10.1029/2020ja028199, 2020.

797 Harvey, V. L., Knox, J. A., France, J. A., Fujiwara, M., Gray, L., Hirooka, T.,

798 Hitchcock, P., Hitchman, M., Kawatani, Y., Manney, G. L., McCormack, J., Orsolini,

799 Y., Sakazaki, T., and Tomikawa, Y.: Chapter 11: Upper Stratosphere and Lower

800   Mesosphere, SPARC Reanalysis Intercomparison Project (S-RIP) Final Report, edited

801   by: Fujiwara, M., Manney, G. L., Gray, L. J., and Wright, J. S., SPARC Report No. 10,

802   WCRP-6/2021, SPARC, DLR-IPA, Oberpfaffenhofen, Germany,

803   https://doi.org/10.17874/800dee57d13, 2021.

804   Harvey, V. L., Randall, C. E., Becker, E., Smith, A. K., Bardeen, C. G., France, J. A.,

805   and Goncharenko, L. P.: Evaluation of the mesospheric polar vortices in WACCM, J.

806   Geophys. Res.-Atmos., 124, 10626–10645, https://doi.org/10.1029/2019jd030727,

807   2019.

808   He, M., Chau, J. L., Stober, G., Li, G., Ning, B., and Hoffmann, P.: Relations between

809   semidiurnal tidal variants through diagnosing the zonal wavenumber using a phase

810   differencing technique based on two ground-based detectors, J. Geophys. Res.-Atmos.,

811   123, 4015–4026, https://doi.org/10.1002/2018jd028400, 2018.

812   He, M., Chau, J. L., Forbes, J. M., Thorsen, D., Li, G., Siddiqui, T. A., Yamazaki, Y.,

813   and Hocking, W. K.: Quasi-10-day wave and semidiurnal tide nonlinear interactions

814   during the Southern Hemispheric SSW 2019 observed in the Northern Hemispheric

815   mesosphere, Geophys. Res. Lett., 47, https://doi.org/10.1029/2020gl091453, 2020a.

816   He, M., Yamazaki, Y., Hoffmann, P., Hall, C. M., Tsutsumi, M., Li, G., and Chau, J. L.:

817   Zonal wave number diagnosis of Rossby wave-like oscillations using paired ground-

818   based radars, J. Geophys. Res.-Atmos., 125, https://doi.org/10.1029/2019jd031599,

819   2020b.

820 Hirooka, T.: Normal mode Rossby waves as revealed by UARS/ISAMS observations, J.

821 Atmos. Sci., 57, 1277–1285, https://doi.org/10.1175/1520-

822 0469(2000)057<1277:NMRWAR>2.0.CO;2, 2000.

823 Holdsworth, D. A., Murphy, D. J., Reid, I. M., and Morris, R. J.: Antarctic meteor

824 observations using the Davis MST and meteor radars, Adv. Space Res., 42, 143–154,

825 https://doi.org/10.1016/j.asr.2007.02.037, 2008.

826 Huang, C., Zhang, S., Chen, G., Zhang, S., and Huang, K.: Planetary wave

827 characteristics in the lower atmosphere over Xianghe (117.00°E, 39.77°N), China,

828 revealed by the Beijing MST radar and MERRA data, J. Geophys. Res.-Atmos., 122,

829 9745–9758, https://doi.org/10.1002/2017jd027029, 2017.

830 Huang, C., Li, W., Zhang, S., Chen, G., Huang, K., and Gong, Y.: Investigation of

831 dominant traveling 10-day wave components using long-term MERRA-2 database,

832 Earth Planets Space, 73, 85, https://doi.org/10.1186/s40623-021-01410-7, 2021.

833 Huang, Y.-Y., Cui, J., Li, H.-J., and Li, C.-Y.: Inter-annual variations of 6.5-day

834 planetary waves and their relations with QBO, Earth Planet. Phys., 6, 135–148,

835 https://doi.org/10.26464/epp2022005, 2022.

836 Jablonowski, C. and Williamson, D. L.: Numerical techniques for global atmospheric

837 models, Lect. Notes Comput. Sci. Eng., 381–493, https://doi.org/10.1007/978-3-642-

838 11640-7_13, 2011.

839 Lee, W., Song, I., Kim, J., Kim, Y. H., Jeong, S., Eswaraiah, S., and Murphy, D. J.: The

840 observation and SD-WACCM simulation of planetary wave activity in the middle

841 atmosphere during the 2019 Southern Hemispheric sudden stratospheric warming, J.

842 Geophys. Res.-Space, 126, https://doi.org/10.1029/2020ja029094, 2021.

843 Lee, W., Lee, C., Kim, J., Kam, H., and Kim, Y. H.: A modeling analysis of the

844 apparent linear relation between mesospheric temperatures and meteor height

845 distributions measured by a meteor radar, J. Geophys. Res.-Space, 127,

846 https://doi.org/10.1029/2021ja029812, 2022.

847 Lee, W., Kim, Y. H., Lee, C., and Wu, Q.: First comparison of mesospheric winds

848 measured with a Fabry-Perot interferometer and meteor radar at the King Sejong Station

849 (62.2°S, 58.8°W), J. Astron. Space Sci., https://doi.org/10.5140/JASS.2018.35.4.235,

850 2018

851 Li, W., Huang, C., and Zhang, S.: Global characteristics of the westward-propagating

852 quasi-16-day wave with zonal wavenumber 1 and the connection with the 2012/2013

853 SSW revealed by ERA-Interim, Earth Planets Space, 73, 113,

854 https://doi.org/10.1186/s40623-021-01431-2, 2021.

855 Lindzen, R. S., Farrell, B., and Tung, K.-K.: The concept of wave overreflection and its

856 application to baroclinic instability, J. Atmos. Sci., 37, 44–63,

857 https://doi.org/10.1175/1520-0469(1980)037<;0044:tcowoa>2.0.co;2, 1980.

858 Liu, G., Janches, D., Lieberman, R. S., Moffat-Griffin, T., Mitchell, N. J., Kim, J., and

859 Lee, C.: Wind variations in the mesosphere and lower thermosphere near 60°S latitude

860 during the 2019 Antarctic sudden stratospheric warming, J. Geophys. Res.-Space, 126,

861 https://doi.org/10.1029/2020ja028909, 2021.

862 Liu, G., Janches, D., Ma, J., Lieberman, R. S., Stober, G., Moffat-Griffin, T., Mitchell,

863 N. J., Kim, J., Lee, C., and Murphy, D. J.: Mesosphere and lower thermosphere winds

864 and tidal variations during the 2019 Antarctic sudden stratospheric warming, J.

865 Geophys. Res.-Space, 127, https://doi.org/10.1029/2021ja030177, 2022.

866 Luo, J., Gong, Y., Ma, Z., Zhang, S., Zhou, Q., Huang, C., Huang, K., Yu, Y., and Li,

867 G.: Study of the quasi 10-day waves in the MLT region during the 2018 February SSW

868 by a meteor radar chain, J. Geophys. Res.-Space, 126,

869 https://doi.org/10.1029/2020ja028367, 2021.

870 Ma, Z., Gong, Y., Zhang, S., Xiao, Q., Xue, J., Huang, C., and Huang, K.:

871 Understanding the excitation of quasi-6-day waves in both hemispheres during the

872 September 2019 Antarctic SSW, J. Geophys. Res.-Atmos., 127,

873 https://doi.org/10.1029/2021jd035984, 2022.

874 Marsh, D. R., Mills, M. J., Kinnison, D. E., Lamarque, J.-F., Calvo, N., and Polvani, L.

875 M.: Climate change from 1850 to 2005 simulated in CESM1(WACCM), J. Climate, 26,

876 130509150556003, https://doi.org/10.1175/jcli-d-12-00558.1, 2013.

877 Matsuno, T.: Vertical propagation of stationary planetary waves in the winter Northern

878 Hemisphere, J. Atmos. Sci., 27, 871–883, https://doi.org/10.1175/1520-

879 0469(1970)027<;0871:vpospw>2.0.co;2, 1970.

880 Matthias, V. and Ern, M.: On the origin of the mesospheric quasi-stationary planetary

881 waves in the unusual Arctic winter 2015/2016, Atmos. Chem. Phys., 18, 4803–4815,

882 https://doi.org/10.5194/acp-18-4803-2018, 2018.

883 Matthias, V., Hoffmann, P., Rapp, M., and Baumgarten, G.: Composite analysis of the

884 temporal development of waves in the polar MLT region during stratospheric

885 warmings, J. Atmos. Sol.-Terr. Phys., 90, 86–96,

886 https://doi.org/10.1016/j.jastp.2012.04.004, 2012.

887 McCormack, J. P., Harvey, V. L., Randall, C. E., Pedatella, N., Koshin, D., Sato, K.,

888 Coy, L., Watanabe, S., Sassi, F., and Holt, L. A.: Intercomparison of middle

889 atmospheric meteorological analyses for the Northern Hemisphere winter 2009–2010,

890 Atmos. Chem. Phys., 21, 17577–17605, https://doi.org/10.5194/acp-21-17577-2021,

891 2021.

892 McFarlane, N. A.: The effect of orographically excited gravity wave drag on the general

893 circulation of the lower stratosphere and troposphere, J. Atmos. Sci., 44, 1775–1800,

894 https://doi.org/10.1175/1520-0469(1987)044<;1775:teooeg>2.0.co;2, 1987.

895 Meyer, C. K. and Forbes, J. M.: A 6.5-day westward propagating planetary wave:

896 Origin and characteristics, J. Geophys. Res.-Atmos., 102, 26173–26178,

897 https://doi.org/10.1029/97jd01464, 1997.

898 Mitra, G., Guharay, A., Batista, P. P., and Buriti, R. A.: Impact of the September 2019

899 minor sudden stratospheric warming on the low-latitude middle atmospheric planetary

900 wave dynamics, J. Geophys. Res.-Atmos., 127, https://doi.org/10.1029/2021jd035538,

901 2022.

902 Palmer, T. N.: Properties of the Eliassen-Palm flux for planetary scale motions, J.

903 Atmos. Sci., 39, 992–997, https://doi.org/10.1175/1520-

904 0469(1982)039<;0992:potepf>2.0.co, 1982.

905 Qin, Y., Gu, S., Dou, X., Gong, Y., Chen, G., Zhang, S., and Wu, Q.: Climatology of

906 the quasi-6-day wave in the mesopause region and its modulations on total electron

907 content during 2003–2017, J. Geophys. Res.-Space, 124, 573–583,

908 https://doi.org/10.1029/2018ja025981, 2019.

909 Qin, Y., Gu, S., Dou, X., Teng, C., Yang, Z., and Sun, R.: Southern Hemisphere

910 response to the secondary planetary waves generated during the Arctic sudden

911 stratospheric final warmings: Influence of the quasi-biennial oscillation, J. Geophys.

912 Res.-Atmos., 127, https://doi.org/10.1029/2022jd037730, 2022.

913 Qin, Y., Gu, S., Teng, C., Dou, X., Yu, Y., and Li, N.: Comprehensive study of the

914 climatology of the quasi-6-day wave in the MLT region based on Aura/MLS

915 observations and SD-WACCM-X simulations, J. Geophys. Res.-Space, 126,

916 https://doi.org/10.1029/2020ja028454, 2021.

917 Reynolds, R. W., Rayner, N. A., Smith, T. M., Stokes, D. C., and Wang, W.: An

918 improved in situ and satellite SST analysis for climate, J. Climate, 15, 1609–1625,

919 https://doi.org/10.1175/1520-0442(2002)015<;1609:aiisas>2.0.co;2, 2002.

920 Rhodes, C. T., Limpasuvan, V., and Orsolini, Y. J.: Eastward-propagating planetary

921 waves prior to the January 2009 sudden stratospheric warming, J. Geophys. Res.-

922 Atmos., 126, https://doi.org/10.1029/2020jd033696, 2021.

923 Richter, J. H., Sassi, F., and Garcia, R. R.: Toward a physically based gravity wave

924 source parameterization in a general circulation model, J. Atmos. Sci., 67, 136–156,

925 https://doi.org/10.1175/2009jas3112.1, 2010.

926 Salby, M. L.: Rossby normal modes in nonuniform background configurations. Part I:

927 Simple fields, J. Atmos. Sci., 38, 1803–1826, https://doi.org/10.1175/1520-

928 0469(1981)038<;1803:rnminb>2.0.co;2, 1981a.

929 Salby, M. L.: Rossby normal modes in nonuniform background configurations. Part II.

930 Equinox and solstice conditions, J. Atmos. Sci., 38, 1827–1840,

931 https://doi.org/10.1175/1520-0469(1981)038<;1827:rnminb>2.0.co;2, 1981b.

932 Salby, M. L.: Survey of planetary-scale traveling waves: The state of theory and

933 observations, Rev. Geophys., 22, 209–236, https://doi.org/10.1029/rg022i002p00209,

934 1984.

935 Sassi, F., McCormack, J. P., Tate, J. L., Kuhl, D. D., and Baker, N. L.: Assessing the

936 impact of middle atmosphere observations on day-to-day variability in lower

937 thermospheric winds using WACCM-X, J. Atmos. Sol.-Terr. Phys., 212, 105486,

938 https://doi.org/10.1016/j.jastp.2020.105486, 2021.

939 Sassi, F. and Liu, H.-L.: Westward traveling planetary wave events in the lower

940 thermosphere during solar minimum conditions simulated by SD-WACCM-X, J.

941 Atmos. Sol.-Terr. Phys., 119, 11–26, https://doi.org/10.1016/j.jastp.2014.06.009, 2014.

942 Sato, K., Yasui, R., and Miyoshi, Y.: The momentum budget in the stratosphere,

943 mesosphere, and lower thermosphere. Part I: Contributions of different wave types and

944 in situ generation of Rossby waves, J. Atmos. Sci., 75, 3613–3633,

945 https://doi.org/10.1175/jas-d-17-0336.1, 2018.

946 Schwartz, M. J., Lambert, A., Manney, G. L., Read, W. G., Livesey, N. J., Froidevaux,

947 L., Ao, C. O., Bernath, P. F., Boone, C. D., Cofield, R. E., Daffer, W. H., Drouin, B. J.,

948 Fetzer, E. J., Fuller, R. A., Jarnot, R. F., Jiang, J. H., Jiang, Y. B., Knosp, B. W.,

949 Krüger, K., Li, J. -L. F., Mlynczak, M. G., Pawson, S., Russell, J. M., Santee, M. L.,

950 Snyder, W. V., Stek, P. C., Thurstans, R. P., Tompkins, A. M., Wagner, P. A., Walker,

951 K. A., Waters, J. W., and Wu, D. L.: Validation of the Aura Microwave Limb Sounder

952 temperature and geopotential height measurements, J. Geophys. Res.-Atmos. 1984

953 2012, 113, https://doi.org/10.1029/2007jd008783, 2008.

954 Song, B.-G., Chun, H.-Y., and Song, I.-S.: Role of gravity waves in a vortex-split

955 sudden stratospheric warming in January 2009, J. Atmos. Sci., 77, 3321–3342,

956 https://doi.org/10.1175/jas-d-20-0039.1, 2020.

957 Thorncroft, C. D., Hoskins, B. J., and McIntyre, M. E.: Two paradigms of baroclinic-

958 wave life-cycle behaviour, Q. J. Roy. Meteor. Soc., 119, 17–55,

959 https://doi.org/10.1002/qj.49711950903, 1993.

960 Torrence, C. and Compo, G. P.: A practical guide to wavelet analysis, B. Am. Meteorol.

961 Soc., 79, 61–78, https://doi.org/10.1175/1520-0477(1998)079<0061:apgtwa>2.0.co;2,

962 1998.

963 Walker, S. N., Sahraoui, F., Balikhin, M. A., Belmont, G., Pinçon, J. L., Rezeau, L.,

964 Alleyne, H., Cornilleau-Wehrlin, N., and André, M.: A comparison of wave mode

965   identification techniques, Ann. Geophys., 22, 3021–3032,

966   https://doi.org/10.5194/angeo-22-3021-2004, 2004.

967   Wang, J. C., Palo, S. E., Forbes, J. M., Marino, J., Moffat-Griffin, T., and Mitchell, N.

968   J.: Unusual Quasi 10-Day Planetary wave activity and the ionospheric response during

969   the 2019 Southern Hemisphere sudden Stratospheric Warming, J. Geophys. Res.-Space,

970   126, https://doi.org/10.1029/2021ja029286, 2021.

971   Yamazaki, Y. and Matthias, V.: Large-amplitude quasi-10-day waves in the middle

972   atmosphere during final warmings, J. Geophys. Res.-Atmos., 124, 9874–9892,

973   https://doi.org/10.1029/2019jd030634, 2019.

974   Yin, S., Ma, Z., Gong, Y., Zhang, S., and Li, G.: Response of quasi-10-day waves in the

975   MLT region to the sudden stratospheric warming in March 2020, Adv. Space Res., 71,

976   298–305, https://doi.org/10.1016/j.asr.2022.10.054, 2023.